



Subpulse Drifting of PSR J1110–5637

S. J. Dang^{1,2}, L. H. Shang^{1,2}, L. Lin³, Q. J. Zhi^{1,2}, R. S. Zhao^{1,2}, C. B. Wu^{1,2}, Z. Y. You^{1,2}, A. J. Dong^{1,2}, J. T. Bai^{1,2}, X. Xu^{1,2},
D. D. Zhang^{1,2}, H. Yang^{1,2}, and Q. W. Lin^{1,2}

¹School of Physics and Electronic Science, Guizhou Normal University, Guiyang 550001, China; dangsj@gznu.edu.cn, qjzhi@gznu.edu.cn

²Guizhou Provincial Key Laboratory of Radio Astronomy and Data Processing, Guizhou Normal University, Guiyang 550001, China

³School of Physics Science and Technology, Xinjiang University, Urumqi 830011, China

Received 2022 January 21; revised 2022 April 12; accepted 2022 April 19; published 2022 May 20

Abstract

We report a detailed study of polarization characteristics and subpulse drifting in PSR J1110–5637 with the observations of the Parkes 64 m radio telescope at 1369 MHz. The observations revealed that the trailing component of the pulse profile has obvious subpulse drifting, while the leading component has no subpulse drifting. Using the two-dimensional fluctuation spectrum (2DFS), we detected three distinct emission modes in the trailing component (modes A, B and C). The emission in mode A is chaotic and indistinguishable, while modes B and C have obvious subpulse drifting. The vertical modulation periods P_3 of modes B and C are around the mean values of $12 P$ and $8 P$, respectively. The subpulse drifting of PSR J1110–5637 will expand the pulsar sample with multiple subpulse drifting rates, and this will help future systematic studies on the physical origin of the subpulse drifting phenomenon.

Key words: (stars:) pulsars: general – (stars:) pulsars: individual (PSR J1110-5637) – Stars

1. Introduction

The single pulse of a pulsar usually consists of one or more subpulse. On observations, for most pulsars, their average pulse profiles are stable. However, the single pulse is variable. The classical pulsar emission variation phenomena mainly include mode changing, nulling, subpulse drifting, giant pulse, giant micropulse, microstructure and so on. Mode changing is the shape of the average pulse profile switches between two or more states (e.g., Backer 1970). Nulling is the emission of a pulsar cannot be detected in several or even thousands of pulse periods (e.g., Wang et al. 2007, 2020). The subpulse drifting is represented by the regular modulation of the subpulse intensity, phase, or both intensity and phase within the average pulse window between successive pulses (e.g., Drake & Craft 1968; Basu et al. 2016). The subpulse drifting bands are usually can be characterized by the horizontal separation between them in pulse longitude (P_2) and the vertical separation in pulse periods (P_3). The slope of the drift bands, $\Delta\phi = \frac{P_2}{P_3}$, is called the drift rate, and it stands for the apparent advance or lag of subpulses per pulse period. In recent years, periodic non-drift intensity modulation has been reported in a number of pulsars (Basu et al. 2016; Yan et al. 2019, 2020; Wen et al. 2020; Kou et al. 2021). The drift rate of these pulsars is $\Delta\phi = 0$. At present, the mode changing, nulling and drifting subpulse are detected in hundreds of pulsars (Wang et al. 2007; Weltevrede et al. 2007; Basu et al. 2019a; Wang et al. 2021; Wen et al. 2022). The observation shows that there may be some connection between these three famous pulsar emission variations. For example, the

subpulse of PSR B0809+74 drifting more slowly after the pulse nulling (van Leeuwen et al. 2003), while the subpulse drifting of PSR B0818–13 appears to speed up during the nulls (Janssen & van Leeuwen 2004).

The subpulse drifting can be roughly classified as four classifications according to the phase behavior of subpulse, coherent phase-modulated drifting, switching phase-modulated drifting, diffuse phase-modulated drifting and low-mixed phase-modulated drifting (Basu et al. 2019a). Subpulse drifting is profile dependent, phase modulation is only shown in the conal components and absent in the central core emission, and amplitude modulation is seen across all components (Basu et al. 2019a). In most cases, mode changing, nulling and subpulse drifting can be explained by the classical “carousel model” (Ruderman & Sutherland 1975). However, for several pulsars, their subpulse drifting shows “Bi-drifting” mode (The main feature of “Bi-drifting” is that the drift rates of different profile components of the same pulsar are different.), such as PSRs J0815+0939 (Champion et al. 2005; Shang et al. 2022), J1034–3224 (Basu & Mitra 2018) and B1839–04 (Szary et al. 2020). In addition, the subpulse in about 10 pulsars have been found to show two or more drifting rates, such as PSRs B0031–07 (Huguenin et al. 1970), J1727–2739 (Wen et al. 2016), B0908+74 (van Leeuwen et al. 2003), B0943+10 (Backus et al. 2011), B1819–22 (Janagal et al. 2022), B1918+19 (Rankin et al. 2013), B1944+17 (Kloumann & Rankin 2010), B2003–08 (Basu et al. 2019b), B2303+30 (Redman et al. 2005) and B2319+60 (Wright & Fowler 1981). Moreover, the probable central core component in the Vela pulsar is measured

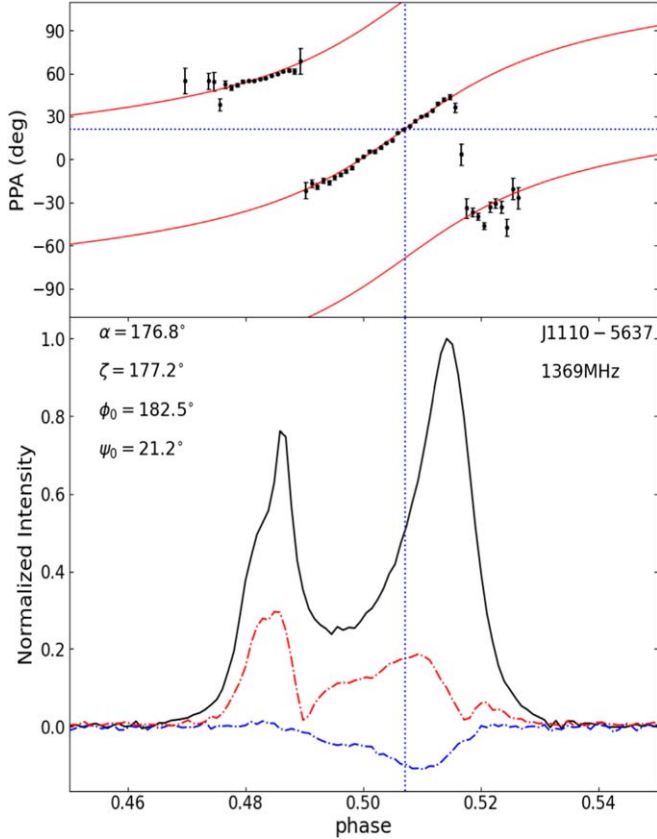


Figure 1. The averaged polarization pulse profile. The bottom panel shows the averaged pulse profile for total intensity (black line), linearly polarized intensity (red line), and circularly polarized intensity (blue line). The top panel gives the position angles of the linearly polarized emission (black dot with error bar) and the best fit to the PA swing (S-shape red solid line). The vertical and horizontal blue dotted lines show the steepest gradient (SG) of the RVM curve at 1369 MHz.

to be modulated both in phase and amplitude (Wen et al. 2020). The above phenomena cannot be well understood by using the classical carousel model.

PSR J1110–5637 (B1107–56) was discovered in the High-frequency Survey of the Southern Galactic Plane for Pulsars by Johnston et al. (1992). The pulsar has a pulse period of $P = 0.5582$ s, the dispersion measure $DM = 262.56 \pm 0.06$ pc cm $^{-3}$ and the characteristic age $\tau_c = 4.29 \times 10^6$ yr. In this paper, we present a detail analysis of subpulse drifting of PSR J1110–5637 with the 1369 MHz observations of the Parkes 64 m radio telescope.

The paper is organized as follows: in Section 2, the observations and data analyses will be introduced. In Section 3, the results, including the pulse profile, subpulse drifting, and energy distribution of single pulses will be presented. Finally, the conclusion and discussion of this paper will be presented in Section 4.

2. Observation and Data Analyses

The observations used in our analyses were made using the Parkes 64 m radio telescope on 2016 April 9 (corresponding to a MJD 57 487). The data was collected by the H-OH receiver (Thomas et al. 1990) in L -band and recorded by the PDFB4. The center frequency is 1369 MHz and the bandwidth is 256 MHz. The data span is 2 h which contain 12,908 subpulse. All of the data were recorded in the PSRFITS (Hotan et al. 2004) format with 8-bit quantization.

First, we downloaded the data from the Parkes Pulsar Data Archive which is publicly available online⁴ (Hobbs et al. 2011). Second, we reduced the data using the DSPSR package (van Straten & Bailes 2011) to de-disperse and form the single-pulse integrations according to the pulsar ephemeris provided by the Australia Telescope National Facility Pulsar Catalogue V1.65⁵ (Manchester et al. 2005). Each single-pulse integration was folded into 1024 phase bins and recorded as the PSRFITS format. Third, the radio frequency interference (RFI) in each data was removed by using the median filtering technique of PAZ plugins of the PSRCHIVE⁶ package (Hotan et al. 2004). 5% of each band edge was zero weighted. The polarization calibration was carried out using the PAC plugin, the calibration steps followed Yan et al. (2011). Finally, the PSRASLA⁷ package (Weltevrede 2016) was used to analyze the fluctuation spectra of the single pulse stacks.

3. Results

3.1. The Averaged Polarization Profile

We analyzed the polarization properties of PSR J1110–5637 at 1369 MHz. Figure 1 shows the averaged polarization pulse profile and polarization position angle of this pulsar. Because there is no calibration for pulsar flux, we only give the normalized pulse profile here. The average linear polarization $L = \sqrt{Q^2 + U^2}$ and circular polarization V are plotted in red and blue lines in the bottom panel, respectively. Significant right-circular polarization is observed in the trailing component. Using the method provided by Zhao et al. (2019), we calculated the pulse width at 10% and 50% of the peak flux density (W_{10} and W_{50}) as well as the separation between two peaks (W_{sp}). It is found that the W_{10} , W_{50} and W_{sp} are 13.70 ± 0.03 (deg), 16.77 ± 0.08 (deg) and 10.48 ± 0.02 (deg), respectively. We also measured the fractional linear polarization L/I , the fractional circular polarization $\langle V \rangle / L$ (where $\langle \rangle$ is the average across the pulse profile window) and the fractional absolute circular polarization $\langle |V| \rangle / L$. The values of L/I , $\langle V \rangle / L$ and $\langle |V| \rangle / L$ are 27%, -7% and 9%, respectively. The polarization profile characteristics of this pulsar are consistent

⁴ <https://data.csiro.au/dap/public/atnf/pulsarSearch.zul>

⁵ <https://data.csiro.au/research/pulsar/psrcat/>

⁶ <http://psrchive.sourceforge.net/>

⁷ <https://github.com/weltevrede/psrsalsa>

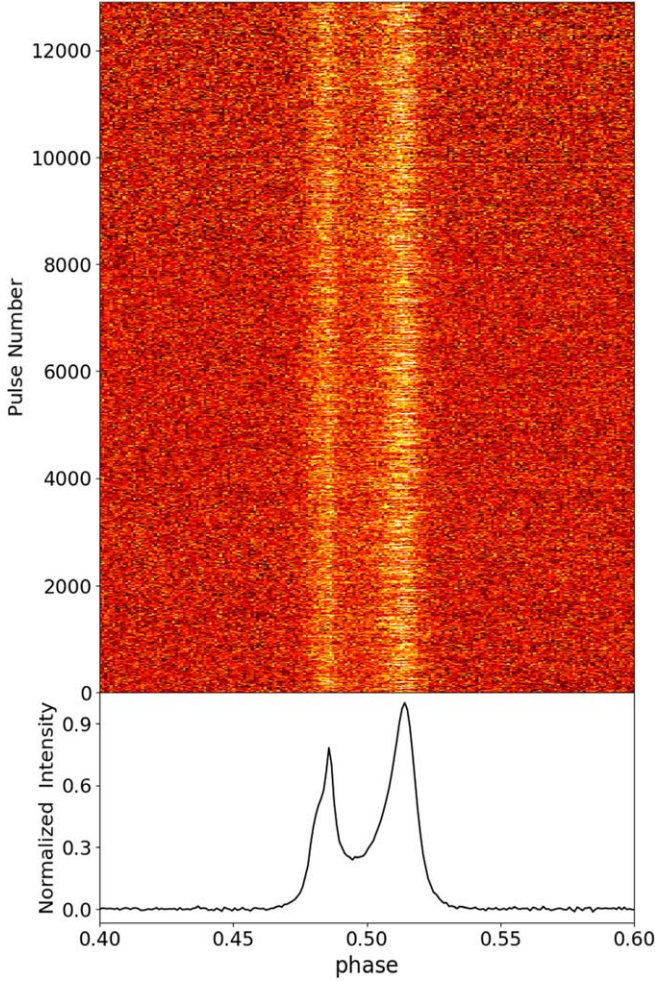


Figure 2. The single pulse stacks comprising of 12,908 consecutive periods for PSR J1110–5637.

with the results in the previously published literature (Johnston & Kerr 2018). The associated polarization position angle (PPA) $\Psi = \frac{1}{2} \arctan\left(\frac{U}{Q}\right)$ is plotted in the top panel. Using the PSRCHIVE tool PSRMODEL⁸, we carried out a rotating vector model (RVM, Radhakrishnan & Cooke 1969) fit to the PPA swing for the average profile. The PPA of the linearly polarized emission, ψ , is a function of α , ζ and the pulse phase, ϕ , according to

$$\tan(\psi - \psi_0) = \frac{\sin(\phi - \phi_0)}{\sin \zeta \cos \alpha - \cos \zeta \sin \alpha \cos(\phi - \phi_0)} \quad (1)$$

where ψ is the PPA, α is the angle between the spin and magnetic axes, ζ is the angle between the spin axis and the line of sight, and ϕ is the phase of the pulsar. The angles ψ_0 and ϕ_0 refer to the PPA at the point of highest rate of change and the

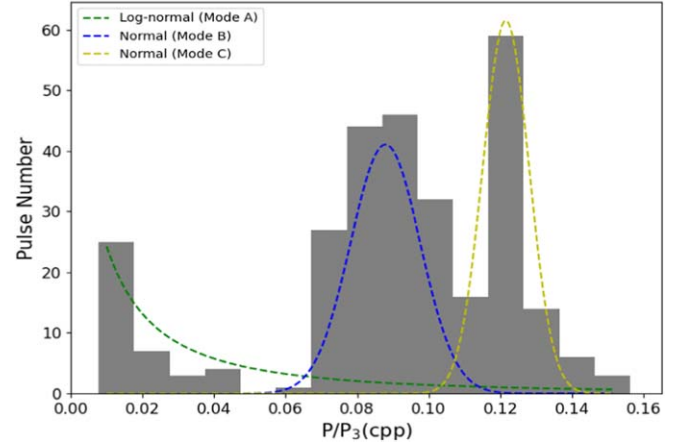


Figure 3. The distribution of P/P_3 values of PSR J1110–5637 as calculated using the PSRSALSA. The green, blue and yellow dashed lines represent the best fit of the distribution of P/P_3 for modes A, B and C, respectively.

corresponding value of ϕ at that point, respectively. The S-shape red solid curve in the top panel in Figure 1 shows the best fit to the PPA with $\alpha = 176^\circ.8$, $\zeta = 177^\circ.2$ and the reduced $\chi^2 = 2.5$. The steepest gradient (SG) of the RVM curve is given by

$$\left(\frac{d\psi}{d\phi}\right)_{\max} = \frac{\sin \alpha}{\sin \beta} \quad (2)$$

(Komesaroff 1970). where the impact parameter $\beta = \zeta - \alpha = 0^\circ.4$. The vertical and horizontal dotted lines in Figure 1 correspond to the point of SG, which with $\phi_0 = 182^\circ.5$ and $\psi_0 = 21^\circ.2$, respectively. The SG can be used to estimate the profile shape. Generally, if the profile have multiple components with core and cone emission, the correspond value of SG will be higher (Lyne & Manchester 1988; Janagal et al. 2022). For this pulsar, it has a double peak profile, and the value of $SG \sim 8^\circ$, which means that it has core and cone components. The trailing component of this pulsar is located near the point of SG, which means that it is from the core emission, while the leading component is from cone emission (e.g., Lyne & Manchester 1988). It is noted that the PPA also shows the presence of two orthogonal polarization modes (OPM, Gil & Lyne 1995), which are 90° jump in the PPA, in both the leading and trailing components. The OPM are believed to be associated with the extraordinary (X) and ordinary (O) modes of the emitting plasma waves (Melikidze et al. 2014).

3.2. Subpulse Drifting

The individual pulse stacks in our observation of PSR J1110–5637 are shown in the top panel of Figure 2 and the corresponding averaged pulse profile is shown in the bottom panel. It is found that the single pulse emission of two components of this pulsar shows obvious variation. Further

⁸ <http://psrchive.sourceforge.net/manuals/psrmodel/>

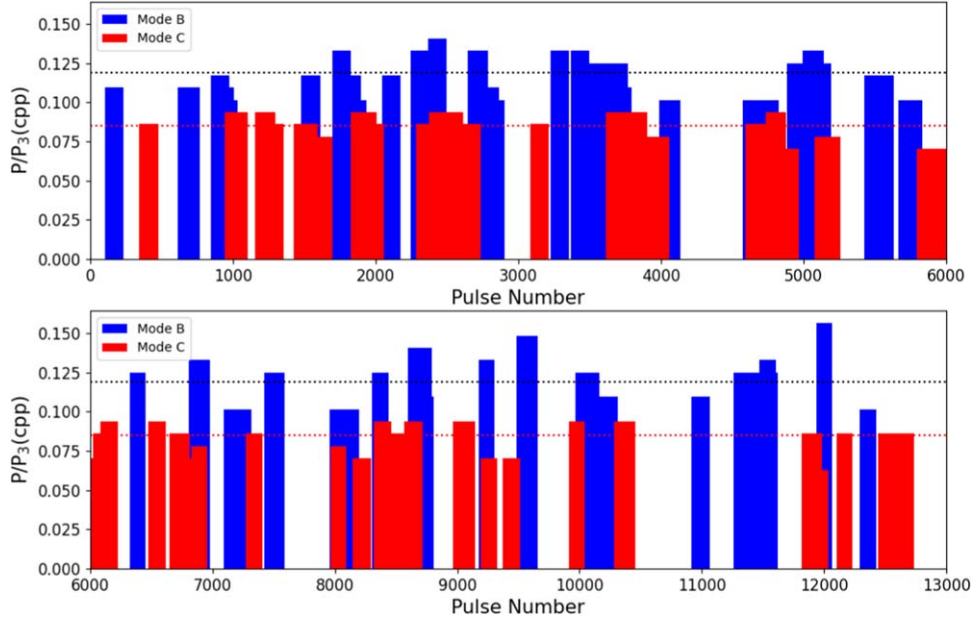


Figure 4. A plot of P/P_3 values of PSR J1110-5637 as calculated using the PSRSALSA software package, where the x -axis shows pulse number and the y -axis shows P/P_3 . The blank areas correspond mode A, and the blue and red bars stand for modes B and C, respectively. The overlap of modes B and C is caused by the overlap of the pulse sequence.

analysis shows that these emission variations are attributed to subpulse drifting. To investigate the detail of the subpulse drifting, we have used the PSRSALSA package to analyze the longitude-resolve modulation index, the longitude-resolved fluctuation spectrum (LRFS) and the two-dimensional fluctuation spectrum (2DFS) of this pulsar (Edwards & Stappers 2002; Weltevrede et al. 2006), respectively. The longitude-resolve modulation index is defined as the factor by which the intensity varies from pulse to pulse, $m_i = \frac{\sigma_i}{\mu_i}$, where, σ_i is the longitude-resolved standard deviation, μ_i is the average intensity at longitude bin i (Weltevrede et al. 2006). The error bars on the modulation index were derived by bootstrapping the data (pulse-stack) (see Weltevrede et al. 2012). The points with error bars is correspond to m_i in the top panel of Figure 6.

Using the LRFS and 2DFS, we can determine values of P_2 and P_3 , respectively. In order to check whether all pulse sequences have the same drifting mode, we adapted the method as Smits et al. (2005) and Rejep et al. (2022) to divide the data into many segments to search P_3 . The difference from the former is that we overlap the data segments in this process. Initially, we selected 100 pulse sequences for each data segment and used PSRSALSA software package for Fourier transform to search P_3 . Once the power spectrum of Fourier transform shows a obvious peak feature, we adjusted the length of the data segment until the signal-to-noise ratio(S/N) is the highest. Here, S/N is the ratio of peak value to the root

mean square value of the rest of the power spectrum. Finally, we find that the S/N is the highest when 150 pulse sequences are used. Therefore, we select that each data segment contains 150 consecutive single pulse sequences and overlaps 140 single pulses. Here, we using 128 as the size of fast Fourier transform (FFT). Figure 3 gives the distribution of the P/P_3 values of the trailing components of data segments with power spectrum $S/N \geq 5$. Obviously, the distribution of the P/P_3 has three peaks. This implies that the subpulse drifting of PSR J1110-5637 may have three modes, A, B and C. Using the least squares fitting, we given the best fit of the P_3 distribution. The P_3 value of mode A is log-normal distribution, with mean value of 0.03 ± 0.04 cycles per period (cpp). Both modes B and C are normal distribution, the correspond mean values are 0.088 ± 0.009 cpp and 0.122 ± 0.006 cpp, respectively. The corresponding P_3 are ~ 33 , 12 and 8 pulse period (P). Based on the best fitting above, we divide the sequence with $P_3 < 0.06$ into mode A, $0.06 < P_3 < 0.11$ into mode B and $P_3 > 0.11$ into mode C. The values of P/P_3 for each data segment are shown in Figure 4. The blank areas correspond to mode A, and the blue and red bars stand for mode B and C, respectively. The red and black dashed lines represent the mean values of P/P_3 of modes B and C, respectively. Overlap of the bars of modes B and C is caused by the overlap of the pulse sequence.

In order to show the drifting pattern more clearly, we selected data segments for each mode and plotted the

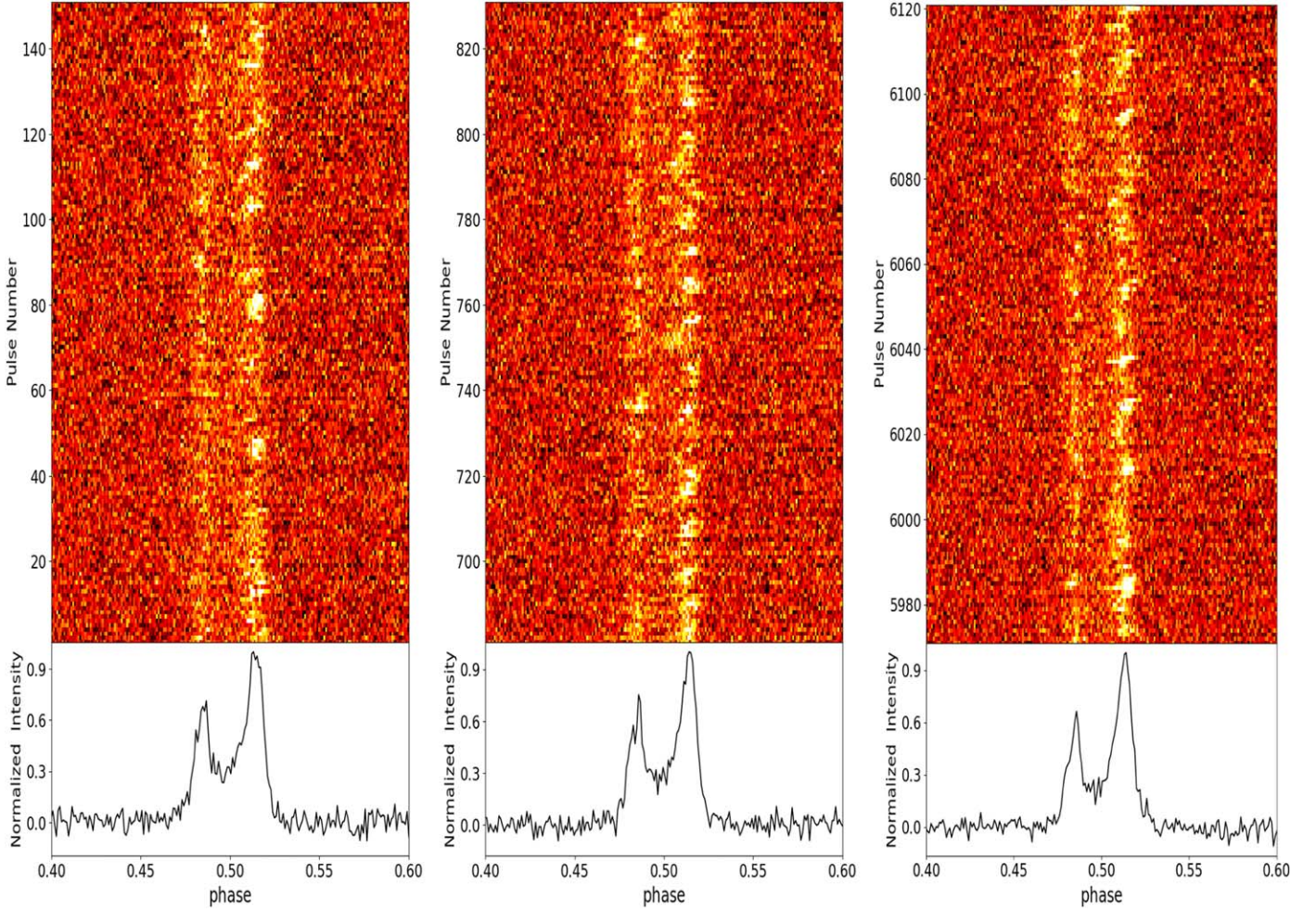


Figure 5. The single pulse stacks and their mean pulse profile of modes A, B, and C. Here we using 150 consecutive single pulse sequences.

corresponding single pulse stacks and their mean pulse profile in Figure 5. It is obvious that the emission of the leading component of the pulse profile for the three modes is weak. For the trailing component, the emission is complex in mode A (It contains discontinuous drifting bands and non-drift subpulse sequences), while the emission has obvious continuous drifting bands in modes B and C. In Figure 6, the analysis of the fluctuation spectra for the trailing component in three modes are presented (the corresponding single pulse sequences are in Figure 5). The units of the horizontally integrated power spectral density of LRFS and 2DFS is P/P_3 and the units of the vertically integrated power spectral density of 2DFS is P/P_2 . From Figure 6, we can see that the LRFS of mode A has a complex spectral feature in the low frequency, while modes B and C have clear spectral features peaking at 0.11 (cpp) and 0.7 (cpp), respectively. Spectral features in modes B and C correspond to the vertical modulation periods of $9.11 P$ and $14.17P$, respectively. Using the PSPECDETECT plugin of

PSRSALSA software package, we have measured the P_2 and P_3 for the well-defined spectral feature for modes B and C. This gives $P_2 = 12 \pm 1(\text{deg})$ and $P_3 = 9.11 \pm 0.04P$ for mode B and $P_2 = 12.6 \pm 0.6(\text{deg})$ and $P_3 = 14.17 \pm 0.07P$ for mode C. It should be noted that although the P_3 of modes B and C are different, the P_2 are the same within the error range. In addition, the 2DFS shows that mode A has a significant P_2 with values of $P_2 = 12 \pm 1(\text{deg})$, this may be from the discontinuous drifting bands.

Furthermore, in order to further check whether the leading component has periodic emission variation behavior invisible to the eye, we plotted the 2DFS of modes A, B and C in Figure 7. Obviously, the leading component of mode A has no obvious P_3 , but has P_2 . This means that the leading component of mode A has no intensity modulation, but has phase modulation. For Modes B and C, the 2DFS of the leading component is dominated by very strong red noise and has no periodicity behavior.

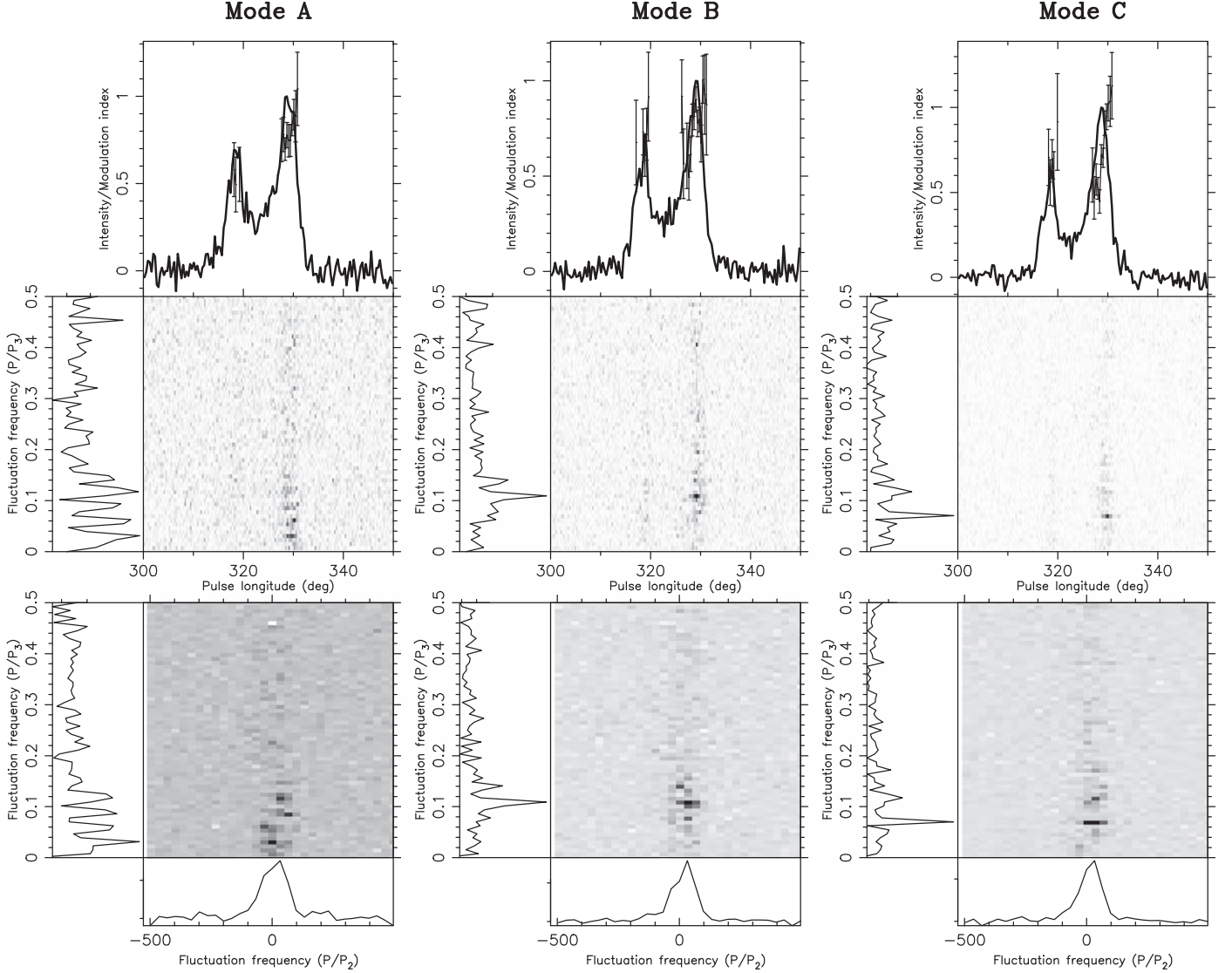


Figure 6. The fluctuation spectral analysis of the trailing component of PSR J1110–5637. Each column corresponds to the fluctuation spectrum of modes A, B and C. The top panel of each column shows the longitude-resolved modulation index and the mean pulse profile. The middle and bottom panels are the LRFS and 2DFS, respectively. The side panels stand for the horizontally (left) and vertically (bottom) integrated power.

3.3. Energy Distribution

In order to statistically check whether the intensity modulation of a single pulse may include a nulling phenomenon, we plot the energy distribution of 12,908 single pulses in Figure 8. Red and black represent on-pulse and off-pulse, respectively. Here, the numbers of phase bin in the on-pulse and off-pulse regions are equal. The blue and purple dotted line represent the best fitting of on-pulse and off-pulse energy based on the single Gaussian mode, respectively. The energy for the on-pulse and off-pulse regions are normalized by the mean pulse energy. As shown in Figure 8, the pulse energy distribution of off-pulse is centered on zero, which is due to

the Gaussian random noise caused by telescope noise. The energy distribution of on-pulse is a Gaussian distribution with a mean value greater than zero, which means that there is no nulling phenomenon in PSR J1110–5637.

4. Conclusion and Discussion

We presented a detailed study of subpulse drifting in PSR J1110–5637 using the observations of Parkes 64 m radio telescope at 1369 MHz, for the first time. We found that the emission of the leading component of this pulsar has irregular variation, while the trailing component has three distinct drifting modes. Mode A shows complex intensity modulation,

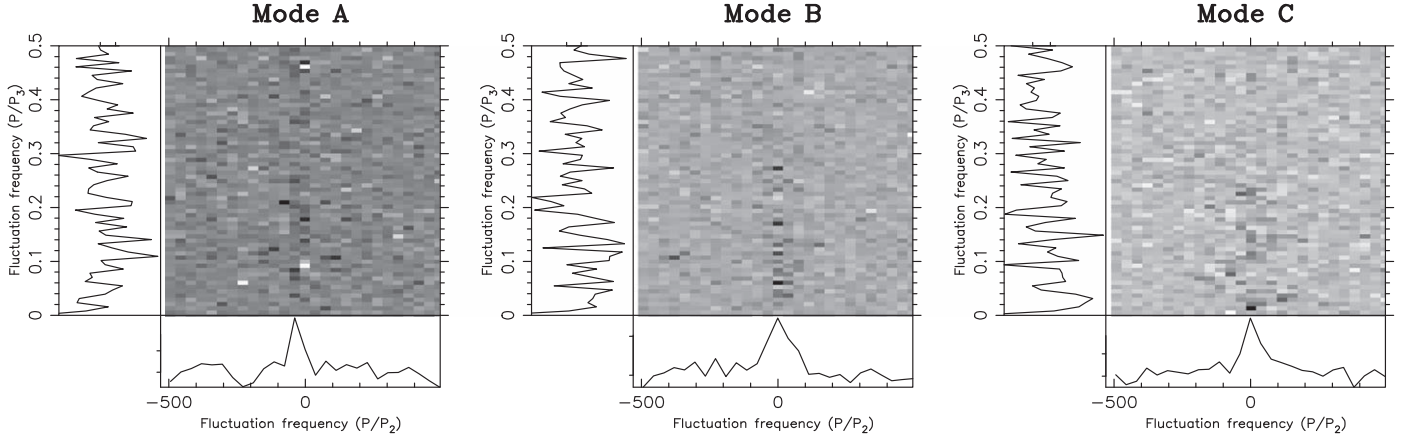


Figure 7. The 2DFS of the leading component of PSR J1110–5637. The side panels stand for the horizontally (left) and vertically (bottom) integrated power. Each column corresponds to modes A, B and C.

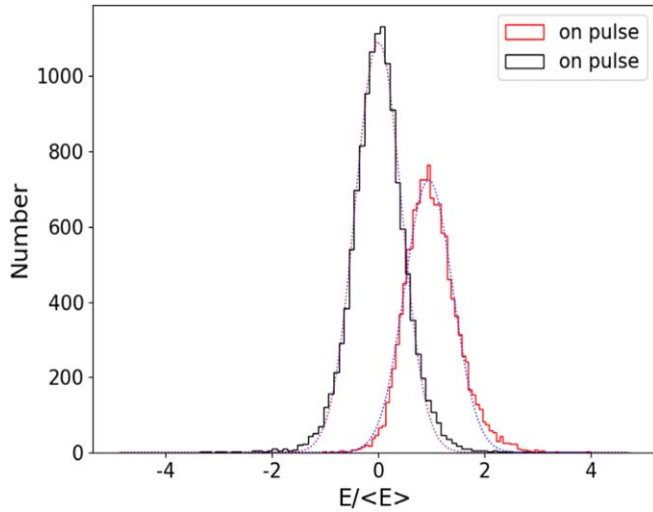


Figure 8. Pulse energy distributions for the on-pulse (red histogram) and off-pulse (black histogram) regions. The blue and purple dotted line represent the best fitting of on-pulse and off-pulse energy based on the single Gaussian mode, respectively. The energies are normalized by the mean on-pulse energy.

while modes B and C have significantly different vertical modulation periods P_3 . The corresponding mean values of P_3 of modes B and C are $12 P$ and $8 P$, respectively.

At present, the most popular model used to explain the subpulse drifting of pulsars is the “carousel model” (Ruderman & Sutherland 1975). The “carousel model” suggested that the emission beam of a pulsar is composed of many small sub-emission beams, which rotate around the magnetic axis under the action of $\mathbf{E} \times \mathbf{B}$ drift force, and the subpulses of pulsar correspond to these sub-emission beams. Due to the motion of the carousel, each sub-emission beam will gradually move forward and sweep the observer’s line of sight, resulting in the

observation of subpulse drifting. Under the framework of this model, the subpulse drifting mode of a pulsar is fixed and does not change with time. However, it is observed that the subpulse drifting of some pulsars shows multiple modes, such as PSR J1110–5637 in this paper. Table 1 shows the statistics of pulsars with multiple subpulse drifting modes, some of the data were collected by Geppert et al. (2021). As Table 1 shows that the multiple subpulse drifting phenomenon has been detected in about 11 pulsars. The multiple subpulse drifting patterns of these pulsars challenge the traditional “carousel model.”

The understanding of the physical origin of multiple subpulse drifting modes is still an open question. Many models have been presented to explain this phenomenon. For instance, the partially screened gap (PSG) model (Gil et al. 2003) considers a partial flow of iron ions from the positively charged polar cap, coexisting with the production of outflowing electron-positron plasma. The model believes that the phenomenon of drifting subpulses is a manifestation of a more general phenomenon related to sparking discharges of the ultra-high potential drop above the polar cap of radio pulsars. Yuen (2019) proposed a model that the changes of subpulse drift rate may be caused by the changes of multiple magnetospheric states incorporating the apparent motion of the visible point. The model of Yuen (2019) is successfully applied to explain the subpulse drifting of PSRs B1819–22, B0809+74 and B1918+19. Geppert et al. (2021) proposed a model based on the Partially Screened Gap (PSG) model of the inner acceleration region (IAR). They suggest that the observed state changes are caused by the Hall and thermoelectric oscillations perturb the polar cap magnetic field to alter the sparking process in the PSG. Using the PSG model, Rahaman et al. (2021) have explained the connection among drifting, mode changing, and nulling of PSR J2321+6024, and suggested that for a variety of surface a non-dipolar magnetic field can explain that the change of the periodic subpulse

Table 1
Pulsars with Multiple Subpulse Drifting Modes

Pulsar B	Pulsar J	Period s	Age yr	B_s G	\dot{E} ergs/s	Subpulse Drifting Modes	P_3	Reference
B0031–07	J0034–0721	0.943	3.66×10^7	6.28×10^{11}	1.9×10^{31}	A	~55 P	(1), (2), (3), (4)
						B	~30 P	
						C	~11 P	
						Null	~32 P	
B0809+74	J0814+7429	1.292	1.22×10^8	4.72×10^{11}	3.1×10^{30}	Normal	~500–1000 P	(5)
						Slow Drift	~100 P	
B0943+10	J0946+0951	1.098	4.98×10^6	1.98×10^{12}	1.0×10^{32}	B	~7.5 hrs	(6)
	J1727–2739	1.293	1.91×10^7	1.19×10^{12}	2.0×10^{31}	Q	~2.2 hrs	(7)
B1819–22	J1822–2256	1.874	2.19×10^7	1.61×10^{12}	8.1×10^{30}	A	9.7 ± 1.6	(8)
						B	5.2 ± 0.9	
						C	...	
						D	17.9 P	
B1918+19	J1921+1948	0.821	1.45×10^7	8.68×10^{11}	6.4×10^{31}	A	5.8 P	(9), (10)
						B	8P	
						C	14.1P	
						D	35 P	
B1944+17	J1946+1805	0.441	2.9×10^8	1.04×10^{11}	1.1×10^{31}	A	53 P	(11), (12)
						B	135 P	
						C	23.5 P	
						D	30–40 P	
B2003–08	J2006–0807	0.580	2×10^8	1.65×10^{11}	9.3×10^{30}	A	10–20 P	(13)
						B	8 P	
						C	11–12 P	
						D	20–100 P	
B2303+30	J2305+3100	1.576	8.63×10^6	2.16×10^{12}	2.9×10^{31}	Null	~100 P	(14)
						B	65 P	
						Q	103 P	
B2319+60	J2321+6024	2.256	5.08×10^6	4.03×10^{12}	2.4×10^{31}	A	16 P	(15)
						B	15 P	
						ABN	~100 P	
B1107–56	J1110–5637	0.558	4.29×10^6	1.09×10^{12}	4.7×10^{32}	A	37 P	This work
						B	31 P	
						C	30–70 P	
						Null	12–15 P	
						ABN	10–15 P	
						C	20–30 P	
						Null	~10 P	
						A	–	
						B	~12 P	
						C	~8 P	

Note. The references are as follows: (1) Huguenin et al. (1970), (2) Vivekanand & Joshi (1997), (3) Smits et al. (2005), (4) McSweeney et al. (2017), (5) van Leeuwen et al. (2003), (6) Backus et al. (2011), (7) Wen et al. (2016), (8) Janagal et al. (2022), (9) Hankins & Wolszczan (1987), (10) Rankin et al. (2013), (11) Deich et al. (1986), (12) Kloumann & Rankin (2010), (13) Basu et al. (2019b), (14) Redman et al. (2005), (15) Wright & Fowler (1981).

drifting may be originated from the changes of a non-dipolar surface magnetic field. Therefore, the PSG model may be used to explain the multiple subpulse drift modes of PSR J1110–5637.

Moreover, Rankin et al. (2013) suggested that aliasing combined with subbeam loss may be responsible for the apparently dramatic changes in drift rates in pulsars. Generally, when the carousel rotation is constant, the observed P_3 should also be constant at any pulse longitude. However, because the subpulses are indistinguishable and we can observe their

positions only once per pulse period, we cannot determine their real speed exactly, which means that the subpulse drifting we observed is aliased (van Leeuwen et al. 2003). McSweeney et al. (2019) show that the changes of subpulse drift rate of PSR B0031–07 can be understood in terms of a single carousel rotation rate if the number of sparks is allowed to change by an integral number, and where the different drift rates are due to (first-order) aliasing effects. Hence, aliasing combined with subbeam loss may also be used to explain the change of drift rate of PSR J1110–5637.

In addition, it is worth noting that the subpulse drifting phenomenon was detected in the possible core component for PSR J1110–5637. This is rare in the pulsar population in previous work. Pulsars exhibiting distinct subpulse drifting modes, such as PSR J1110–5637, will give a unique opportunity to study the physical mechanism of these phenomena. Due to the limit of sensitivity, we cannot study the subpulse drifting of this pulsar with a high signal-to-noise ratio. We look forward to the Parkes UWL receiver or Square Kilometer Array (SKA) to observe this pulsar in the future to help us understand the physical mechanism of the multiple subpulse drifting modes.

Acknowledgments

We thank Wenming Yan and Jumei Yao for useful discussion. This work was supported by Guizhou Province Science and Technology Foundation (No. ZK[2022]304), the National Natural Science Foundation of China (Nos. U1731238, 11565010, 12103013 and U1831120), the Foundation of Guizhou Provincial Education Department (No. KY(2020)003 and KY(2021)303). The Parkes radio telescope is part of the Australia Telescope National Facility which is funded by the Commonwealth of Australia for operation as a National Facility managed by CSIRO. This paper includes archived data obtained through the CSIRO Data Access Portal.

References

- Backer, D. C. 1970, *Natur*, **228**, 1297
- Backus, I., Mitra, D., & Rankin, J. M. 2011, *MNRAS*, **418**, 1736
- Basu, R., & Mitra, D. 2018, *MNRAS*, **475**, 5098
- Basu, R., Mitra, D., Melikidze, G. I., et al. 2016, *ApJ*, **833**, 29
- Basu, R., Mitra, D., Melikidze, G. I., & Skrzypczak, A. 2019a, *MNRAS*, **482**, 3757
- Basu, R., Paul, A., & Mitra, D. 2019b, *MNRAS*, **486**, 5216
- Champion, D. J., Lorimer, D. R., McLaughlin, M. A., et al. 2005, *MNRAS*, **363**, 929
- Deich, W. T. S., Cordes, J. M., Hankins, T. H., & Rankin, J. M. 1986, *ApJ*, **300**, 540
- Drake, F. D., & Craft, H. D. 1968, *Natur*, **220**, 231
- Edwards, R. T., & Stappers, B. W. 2002, *A&A*, **393**, 733
- Geppert, U., Basu, R., Mitra, D., Melikidze, G. I., & Szkudlarek, M. 2021, *MNRAS*, **504**, 5741
- Gil, J., Melikidze, G. I., & Geppert, U. 2003, *A&A*, **407**, 315
- Gil, J. A., & Lyne, A. G. 1995, *MNRAS*, **276**, L55
- Hankins, T. H., & Wolszczan, A. 1987, *ApJ*, **318**, 410
- Hobbs, G., Miller, D., Manchester, R. N., et al. 2011, *PASA*, **28**, 202
- Hotan, A. W., van Straten, W., & Manchester, R. N. 2004, *PASA*, **21**, 302
- Huguenin, G. R., Taylor, J. H., & Troland, T. H. 1970, *ApJ*, **162**, 727
- Janagal, P., Chakraborty, M., Bhat, N. D. R., Bhattacharyya, B., & McSweeney, S. J. 2022, *MNRAS*, **509**, 4573
- Janssen, G. H., & van Leeuwen, J. 2004, *A&A*, **425**, 255
- Johnston, S., & Kerr, M. 2018, *MNRAS*, **474**, 4629
- Johnston, S., Lyne, A. G., Manchester, R. N., et al. 1992, *MNRAS*, **255**, 401
- Kloumann, I. M., & Rankin, J. M. 2010, *MNRAS*, **408**, 40
- Komesaroff, M. M. 1970, *Natur*, **225**, 612
- Kou, F. F., Yan, W. M., Peng, B., et al. 2021, *ApJ*, **909**, 170
- Lyne, A. G., & Manchester, R. N. 1988, *MNRAS*, **234**, 477
- Manchester, R. N., Hobbs, G. B., Teoh, A., & Hobbs, M. 2005, *AJ*, **129**, 1993
- McSweeney, S. J., Bhat, N. D. R., Tremblay, S. E., Deshpande, A. A., & Ord, S. M. 2017, *ApJ*, **836**, 224
- McSweeney, S. J., Bhat, N. D. R., Wright, G., Tremblay, S. E., & Kudale, S. 2019, *ApJ*, **883**, 28
- Melikidze, G. I., Mitra, D., & Gil, J. 2014, *ApJ*, **794**, 105
- Radhakrishnan, V., & Cooke, D. J. 1969, *Astrophys. Lett.*, **3**, 225
- Rahaman, S. k. M., Basu, R., Mitra, D., & Melikidze, G. I. 2021, *MNRAS*, **500**, 4139
- Rankin, J. M., Wright, G. A. E., & Brown, A. M. 2013, *MNRAS*, **433**, 445
- Redman, S. L., Wright, G. A. E., & Rankin, J. M. 2005, *MNRAS*, **357**, 859
- Rejep, R., Wang, N., Yan, W. M., & Wen, Z. G. 2022, *MNRAS*, **509**, 2507
- Ruderman, M. A., & Sutherland, P. G. 1975, *ApJ*, **196**, 51
- Shang, L.-H., Bai, J.-T., Dang, S.-J., & Zhi, Q.-J. 2022, *RAA*, **22**, 025018
- Smits, J. M., Mitra, D., & Kuijpers, J. 2005, *A&A*, **440**, 683
- Szary, A., van Leeuwen, J., Weltevrede, P., & Maan, Y. 2020, *ApJ*, **896**, 168
- Thomas, B. M., Greene, K. J., & James, G. L. 1990, *ITAP*, **38**, 1898
- van Leeuwen, A. G. J., Stappers, B. W., Ramachandran, R., & Rankin, J. M. 2003, *A&A*, **399**, 223
- van Straten, W., & Bailes, M. 2011, *PASA*, **28**, 1
- Vivekanand, M., & Joshi, B. C. 1997, *ApJ*, **477**, 431
- Wang, N., Manchester, R. N., & Johnston, S. 2007, *MNRAS*, **377**, 1383
- Wang, P. F., Han, J. L., Han, L., et al. 2020, *A&A*, **644**, A73
- Wang, Z., Wen, Z. G., Yuan, J. P., et al. 2021, *ApJ*, **923**, 259
- Weltevrede, P. 2016, *A&A*, **590**, A109
- Weltevrede, P., Edwards, R. T., & Stappers, B. W. 2006, *A&A*, **445**, 243
- Weltevrede, P., Stappers, B. W., & Edwards, R. T. 2007, *A&A*, **469**, 607
- Weltevrede, P., Wright, G., & Johnston, S. 2012, *MNRAS*, **424**, 843
- Wen, Z. G., Chen, J. L., Hao, L. F., et al. 2020, *ApJ*, **900**, 168
- Wen, Z. G., Wang, N., Yuan, J. P., et al. 2016, *A&A*, **592**, A127
- Wen, Z. G., Yuan, J. P., Wang, N., et al. 2022, *ApJ*, **929**, 71
- Wright, G. A. E., & Fowler, L. A. 1981, *A&A*, **101**, 356
- Yan, W. M., Manchester, R. N., van Straten, W., et al. 2011, *MNRAS*, **414**, 2087
- Yan, W. M., Manchester, R. N., Wang, N., et al. 2019, *MNRAS*, **485**, 3241
- Yan, W. M., Manchester, R. N., Wang, N., et al. 2020, *MNRAS*, **491**, 4634
- Yuen, R. 2019, *MNRAS*, **486**, 2011
- Zhao, R.-S., Yan, Z., Wu, X.-J., et al. 2019, *ApJ*, **874**, 64